Chinese Journal of Aeronautics, (2024), 37(2): 431–445

Chinese Society of Aeronautics and Astronautics
& Beihang University

Chinese Journal of Aeronautics

cja@buaa.edu.cn
www.sciencedirect.com

FULL LENGTH ARTICLE

Wind disturbance compensated path-following control for fixed-wing UAVs in arbitrarily strong winds

Hao LU [a], **Lan GAO** [b,*], **Yunda YAN** [c], **Mingzhe HOU** [d], **Chenliang WANG** [e]

[a] *Hangzhou Innovation Institute, Beihang University, Hangzhou 310051, China*
[b] *School of Information Science and Technology, Hangzhou Normal University, Hangzhou 311121, China*
[c] *Department of Computer Science, University College London, London WC1E 6BT, United Kingdom*
[d] *Center for Control Theory and Guidance Technology, Harbin Institute of Technology, Harbin 150001, China*
[e] *School of Automation Science and Electrical Engineering, Beihang University, Beijing 100191, China*

Received 14 February 2023; revised 17 April 2023; accepted 4 June 2023
Available online 26 September 2023

KEYWORDS

Path following;
Guiding vector field;
Wind disturbance;
Disturbance rejection;
Fixed wings

Abstract Wind is the primary challenge for low-speed fixed-wing unmanned aerial vehicles to follow a predefined flight path. To cope with various wind conditions, this paper proposes a wind disturbance compensated path following control strategy where the wind disturbance estimate is incorporated with the nominal guiding vector field to provide the desired airspeed direction for the inner-loop. Since the control input vector for the outer-loop kinematic subsystem needs to satisfy a magnitude constraint, a scaling mechanism is introduced to tune the proportions of the compensation and nominal components. Moreover, an optimization problem is formulated to pursue a maximum wind compensation in strong winds, which can be solved analytically to yield two scaling factors. A cascaded inner-loop tracking controller is also designed to fulfill the outer-loop wind disturbance compensated guiding vector field. High-fidelity simulation results under sensor noises and realistic winds demonstrate that the proposed path following algorithm is less sensitive to sensor noises, achieves promising accuracy in normal winds, and mitigates the deviation from a desired path in wild winds.

1. Introduction

Recent years have witnessed increasing applications of fixed-wing Unmanned Aerial Vehicles (UAVs) in various fields such as surveillance, reconnaissance, patrol, mapping, etc. In these tasks, fixed-wing UAVs are often required to precisely move along a predefined path, while the speed assignment along the path is of secondary interest, which leads to so-called path fol-

* Corresponding author.
E-mail address: langao@hznu.edu.cn (L. GAO).
Peer review under responsibility of Editorial Committee of CJA.

https://doi.org/10.1016/j.cja.2023.09.020

lowing problems. Compared to another motion control pattern of trajectory tracking, which commands the vehicle to track a time-parameterized reference, path following focuses on staying on the path without a temporal requirement. Detailed performance comparisons have been made between path following and trajectory tracking, which indicate smaller position errors for path following.[1,2] When applied to fixed-wing UAVs, path following is more suitable because the speed control response is relatively slow and the airspeed needs to be controlled in a desired range for saving energy and preventing stall.

Comparisons of several baseline path following techniques for fixed-wing UAVs can be found in Refs. 3,4. It was concluded that the vector field technique achieved lower cross-tracking error and also used less control effort, which makes it suitable for situations that demand more accuracy and endurance. Another survey paper described that vector field method is more flexible to be extended to deal with obstacle avoidance.[5] The general vector field presented in Refs. 3,6 is only applicable to straight lines and circular orbits in the horizontal plane. By using the cross-tracking error expressed in the Serret-Frenet frame, Ref. 7 developed the vector field for a horizontal curved path. Recently, more generic guiding vector field for Three-Dimensional (3D) curves have been developed.[8,9] In Ref. 9, the desired 3D path can be defined in the parameterized explicit form which is more straightforward than using the intersection of implicit functions.[8] Moreover, to eliminate the undesired singular point where the vector field becomes 0, Ref. 9 proposed a solution of changing the topology of the desired path by introducing a virtual axis. More theoretical analysis about global convergence to the desired path can be found in Ref. 10. So far, the advantages of lower cross-track error and being suitable for complicated 3D curves make the singularity-free guiding vector field a superior method to construct the path following algorithm for fixed-wing UAVs.

The most significant external adverse influence on a fixed-wing aircraft originates from wind.[11] Especially for small-scaled fixed-wing UAVs, the external wind can cause an apparent derivation between the airspeed and the ground speed because the wind speed is generally in the range of 20 to 50 percent of the airspeed.[6] Thus, the elimination of wind effects should be deliberately considered in path following studies. One solution is to employ the ground speed and related flight path angles, as adopted in the vector field based path following designs,[9,12,13] because the ground speed determines the actual flight path. However, in practice, for small-scaled UAVs equipped with a low-cost sensor suit, the ground speed related measurements may not be of good quality due to the low-rate and intermittent Global Navigation Satellite System (GNSS) signal, whereas the airspeed is a more smooth and reliable measurement. Since the airspeed is an essential variable involved in all aerodynamic forces and moments through dynamic pressure, it is also more effective to control the airspeed rather than the ground speed, for example, to avoid undesired stall or save energy.

If the guidance model is expressed in terms of the airspeed related variables, the wind disturbance must be handled explicitly. To acquire the robustness against winds, Ref. 7 adopted the sliding mode method to attenuate the wind disturbance. What's more, various methods can be used for wind estimation, such as adaptive method,[14] extended Kalman filter,[15] nonlinear state observer,[16] and disturbance observers.[17–19] Mostly, wind estimates were used to complement the guidance model and treated as the known parameters in the nonlinear controllers. As for the explicit wind compensation, since there is a miss-matching problem between the wind disturbance and the control input, Ref. 17 converted wind estimates to trimming angles to neutralize the wind components perpendicular to the path.

To our knowledge, the existing 3D guiding vector field overlooks the airspeed and only focuses on ground tracking. Thus, there is still plenty of room to improve the guiding vector field by using airspeed measurement and explicitly taking wind into account. We advocate the Disturbance Observer Based Control (DOBC) scheme to estimate and then compensate for the wind disturbance. This method has been considered popular in disturbance rejection and also has been successfully applied in various tracking control designs, such as helicopter,[20] quadrotor,[21] fixed-wing aircraft,[22] inertial actuator,[23] and spacecraft.[24] When applied to the outer-loop kinematic subsystem, which is Multi-Input Multi-Output (MIMO), the first column of the rotation matrix is chosen as the control input vector, which has a norm constraint of 1. Thus, the feed-forward compensation for the wind disturbance cannot be directly added to the nominal control input. However, how to satisfy the magnitude constraint of the control input vector for a MIMO system has not been explored in the previous DOBC works.[25]

Particularly, considering some low-speed fixed-wing UAVs, e.g., solar-powered UAVs, it is very likely that the wind speed rises close to the airspeed or even above it under extreme wind conditions. In such circumstances, ensuring a safe flight has a higher priority than keeping the UAV on the path. However, all the path following algorithms mentioned above do not discuss this problem. In Refs. 26,27, a geometric guidance law was proposed, which can mitigate the run-away from the desired path in excess winds. Although the guidance command is continuous to wind changes, the guidance law is separately designed for the slower wind case and the higher wind case. Moreover, how to evaluate the performance of the guidance logic in excess winds is still an open problem.

With the above motivations, a wind disturbance compensated guiding vector field is proposed for the fixed-wing UAV path-following control. The main contributions of this paper are summarized as follows.

(1) In order to satisfy the magnitude constraint of the control input vector, a scaling mechanism is first introduced to dynamically tune the proportions of the nominal control input and the disturbance compensation in the DOBC scheme. The scaling factors can be derived by analytically solving an optimization problem which is designed to give the first priority to the disturbance compensation.
(2) The proposed wind disturbance compensated guiding vector field can provide airspeed direction guidance command by integrating guiding vector field with an explicit estimation and rejection of the wind disturbance. Simulation results show that, compared with the original guiding vector field,[9] the proposed algorithm has better sensor noise tolerance and consequently achieves better following accuracy in normal wind conditions.

(3) The proposed wind disturbance compensated guiding vector field is also appropriate for wild winds, which is beyond the reach of the original guiding vector field. Compared with the geometric guidance logic,[26] the proposed algorithm is presented in a unified framework for arbitrarily strong wind conditions and demonstrates better performance in minimizing the deviation from the desired path.

In addition, many existing studies on the path following technique are only concerned with the outer-loop guidance design and assume that the inner-loop controller is well-designed to track the guidance commands (e.g., Refs. 7,9,18). However, the specific guidance commands generated by advanced guiding algorithms may have different requirements on the inner-loop controller so that guidance and control are recommended to be designed in a unified framework as stated in Refs. 28,29. Thus, this paper constructs the overall path following control strategy based on a six-Degree-of-Freedom (6-DOF) nonlinear model, and the inner-loop tracking controller is coherently designed with the outer-loop wind disturbance compensated guiding vector field.

The remainder of this paper is organized as follows. The kinematics of fixed-wing UAVs and the original guiding vector field are presented in Section 2. The detailed wind disturbance compensated guiding vector field design is introduced in Section 3. Section 4 is devoted to developing the inner-loop tracking controller. Section 5 presents the simulation results to demonstrate the effectiveness of the proposed wind disturbance compensated path following algorithm, which is followed by the conclusions drawn in Section 6.

2. Problem formulation

2.1. Kinematics of fixed-wing UAVs

To describe the kinematics of fixed-wing UAVs, four coordinate frames are used: the vehicle carried North-East-Down (NED) frame $\mathcal{F}^{\mathrm{v}}$, the body frame $\mathcal{F}^{\mathrm{b}}$, the flight-path frame $\mathcal{F}^{\mathrm{p}}$, and the air-mass frame $\mathcal{F}^{\mathrm{a}}$, which are all defined according to the right-hand rule. The configuration of frames and variables are briefly shown in Fig. 1, where $\boldsymbol{i}$, $\boldsymbol{j}$, and $\boldsymbol{k}$ are unit vectors along the x, y, and z axes, respectively. Subscripts are used to denote the labels of each frame. For example, $\mathcal{F}^{\mathrm{v}}$ frame is specified by $(\boldsymbol{i}^{\mathrm{v}}, \boldsymbol{j}^{\mathrm{v}}, \boldsymbol{k}^{\mathrm{v}})$ and $\mathcal{F}^{\mathrm{b}}$ frame is specified by $(\boldsymbol{i}^{\mathrm{b}}, \boldsymbol{j}^{\mathrm{b}}, \boldsymbol{k}^{\mathrm{b}})$. The $\boldsymbol{i}$-axes of $\mathcal{F}^{\mathrm{p}}$ and $\mathcal{F}^{\mathrm{a}}$ point along the ground speed vector $\boldsymbol{V}_{\mathrm{g}}$ and the airspeed vector $\boldsymbol{V}_{\mathrm{a}}$, respectively. $\boldsymbol{V}_{\mathrm{a}}$, $\boldsymbol{V}_{\mathrm{g}}$, and the wind speed vector $\boldsymbol{W}$ form the wind triangle. The flight-path angle γ and course angle χ are used to represent the rotations from $\mathcal{F}^{\mathrm{v}}$ to $\mathcal{F}^{\mathrm{p}}$. Similarly, the air-mass-referenced γ_{a} and χ_{a} are rotation angles from $\mathcal{F}^{\mathrm{v}}$ to $\mathcal{F}^{\mathrm{a}}$. ψ, θ, and ϕ are Euler rotation angles.

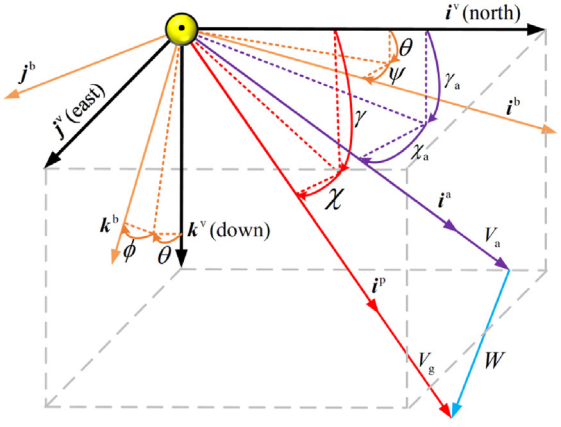

Fig. 1 Illustration of coordinate frames.

The translational kinematics of fixed-wing UAVs can be expressed as

$$\dot{\boldsymbol{P}} = \boldsymbol{V}_{\mathrm{g}} = V_{\mathrm{g}} \mathscr{R}_{\mathrm{p}}^{\mathrm{v}} \boldsymbol{i} \tag{1}$$

When explicitly considering wind effects, Eq. (1) can be rewritten as[6,30]

$$\dot{\boldsymbol{P}} = \boldsymbol{V}_{\mathrm{g}} = V_{\mathrm{a}} \mathscr{R}_{\mathrm{a}}^{\mathrm{v}} \boldsymbol{i} + \boldsymbol{W} \tag{2}$$

where $\boldsymbol{P}$ is the position vector resolved in $\mathcal{F}^{\mathrm{v}}$. $\boldsymbol{i} = [1,\ 0,\ 0]^{\mathrm{T}}$ extracts the first column of the rotation matrix, such that

$$\mathscr{R}_{\mathrm{p}}^{\mathrm{v}} \boldsymbol{i} = \begin{bmatrix} \cos\gamma\cos\chi \\ \cos\gamma\sin\chi \\ -\sin\gamma \end{bmatrix},\quad \mathscr{R}_{\mathrm{a}}^{\mathrm{v}} \boldsymbol{i} = \begin{bmatrix} \cos\gamma_a\cos\chi_a \\ \cos\gamma_a\sin\chi_a \\ -\sin\gamma_a \end{bmatrix}$$

2.2. Original singularity-free guiding vector field

Consider the desired 3D path $\mathscr{P} \in \mathbb{R}^3$ described by the following explicit equation:

$$\mathscr{P} = \{(x,\ y,\ z):\ x = f_1(\tau w),\ y = f_2(\tau w),\ z = f_3(\tau w)\} \tag{3}$$

where $w \in \mathbb{R}$ is the variable of the path, $\tau > 0$ is a constant, and the functions f_i (i =1,2,3) belong to C^2 space.

Therefore, the path following errors can be defined by the functions

$$\begin{cases} \varphi_1(\xi) = x - f_1(\tau w) \\ \varphi_2(\xi) = y - f_2(\tau w) \\ \varphi_3(\xi) = z - f_3(\tau w) \end{cases} \tag{4}$$

and stacking φ_i yields the error vector

$$\boldsymbol{e}(\xi) = [\varphi_1(\xi),\ \varphi_2(\xi),\ \varphi_3(\xi)]^{\mathrm{T}}$$

where $\xi = (x,\ y,\ z,\ w)$ is the augmented position vector with an additional coordinate w, compared to $\boldsymbol{P}$. A new higher-dimensional desired path can be characterized by the zero-following error as

$$\mathscr{P}_{\mathrm{h}} = \left\{\xi \in \mathbb{R}^4:\ \boldsymbol{e}(\xi) = 0\right\}$$

Following Ref. 9, the corresponding singularity-free guiding vector field for $\mathscr{P}_{\mathrm{h}}$ can be constructed as

$$\dot{\xi}_{\mathrm{d}} = \times(\rho\nabla\varphi_1,\ \rho\nabla\varphi_2,\ \rho\nabla\varphi_3) - \sum_{i=1}^{3} k_i \rho\varphi_i \rho\nabla\varphi_i \tag{5}$$

where $\nabla\varphi_i$ is the gradient of the function φ_i, $\rho \in (0, 1)$ is the coefficient of φ, $k_i > 0$ ($i = 1,\ 2,\ 3$) are constant gains, and $\times(\cdot)$ represents the generalized cross product of $\nabla\varphi_1$, $\nabla\varphi_2$, and $\nabla\varphi_3$. Substituting $\nabla\varphi_1 = \left[1,\ 0,\ 0,\ -\tau f_1'(\tau w)\right]^{\mathrm{T}}$,

$\nabla\varphi_2 = [1,\ 0,\ 0,\ -\tau f_2'(\tau w)]^{\mathrm{T}}$, and $\nabla\varphi_3 = [1,\ 0,\ 0,\ -\tau f_3'(\tau w)]^{\mathrm{T}}$. Eq. (6) can be further derived as

$$\dot{\xi}_{\mathrm{d}} = \begin{bmatrix} -\rho^3\tau f_1'(\tau w) - k_1\rho^2\varphi_1(\xi) \\ -\rho^3\tau f_2'(\tau w) - k_2\rho^2\varphi_2(\xi) \\ -\rho^3\tau f_3'(\tau w) - k_3\rho^2\varphi_3(\xi) \\ -\rho^3 + \rho^2\tau\left(k_1\varphi_1(\xi)f_1'(\tau w) + k_2\varphi_2(\xi)f_2'(\tau w) + k_3\varphi_3(\xi)f_3'(\tau w)\right) \end{bmatrix} \tag{6}$$

2.3. Path following control objective

The vectors in the field serve as speed direction commands to the vehicle. The first three entries of vector field $\dot{\xi}_{\mathrm{d}}$ can be used to define the desired ground speed direction using the normalized vector

$$\bar{\boldsymbol{P}}_{\mathrm{d}} = \bar{\boldsymbol{V}}_{\mathrm{g,\,d}} = \frac{\dot{\xi}_{\mathrm{d}}(1:3)}{\|\ \dot{\xi}_{\mathrm{d}}(1:3)\ \|} \tag{7}$$

based on the condition $\dot{\xi}_{\mathrm{d}}(1:3) \neq \boldsymbol{0}$.

Remark 1. Although $\dot{\xi}_{\mathrm{d}} \neq \boldsymbol{0}$ was proved in Ref. 9, which implies that there are no singular points in the higher-dimensional space $\mathbb{R}^4$, it cannot guarantee that $\dot{\xi}_{\mathrm{d}}(1:3) \neq \boldsymbol{0}$ is true for any point $\xi \in \mathbb{R}^4$. Since fixed-wing UAVs always hold a forward speed and never stop at a specific point, we can formulate a strategy that when coming across a point that makes $\dot{\xi}_{\mathrm{d}}(1:3) = \boldsymbol{0}$, $\bar{\boldsymbol{P}}_{\mathrm{d}}$ will keep the last valid value to avoid singularity.

If the vehicle follows the vector direction, it will follow the path. Conceptually, based on Eq. (1), the path following control objective is to orient the ground speed direction $\mathscr{R}_{\mathrm{p}}^{\mathrm{v}}\boldsymbol{i}$ along $\bar{\boldsymbol{P}}_{\mathrm{d}}$. As discussed in Section 1, the ground speed related variables derived from the external GNSS data may be degraded due to environment or interference and airspeed measurement is more reliable. Hence, when we want to manipulate the airspeed direction instead of the ground speed direction, according to Eq. (2), the control objective changes to

$$\frac{V_{\mathrm{a}}\mathscr{R}_{\mathrm{a}}^{\mathrm{v}}\boldsymbol{i} + \boldsymbol{W}}{\|\ V_{\mathrm{a}}\mathscr{R}_{\mathrm{a}}^{\mathrm{v}}\boldsymbol{i} + \boldsymbol{W}\ \|} \rightarrow \bar{\boldsymbol{P}}_{\mathrm{d}} \tag{8}$$

Since the magnitude of the airspeed needs to be controlled in a limited range to prevent stall, the airspeed controller is usually designed independently and not considered in the path following control pattern.[2,3] The airspeed direction represented by $\mathscr{R}_{\mathrm{a}}^{\mathrm{v}}\boldsymbol{i}$ is used as the control variable to achieve the control objective. Obviously, the problems that the wind speed $\boldsymbol{W}$ is unknown and there is a magnitude constraint $\|\ \mathscr{R}_{\mathrm{a}}^{\mathrm{v}}\boldsymbol{i}\ \| = 1$ should be dealt with in the path following controller design.

3. Wind disturbance compensated guiding vector field

In this section, the wind disturbance guiding vector field for the outer-loop guidance is proposed. A disturbance observer is employed to estimate the composite wind disturbance, and then a feed-forward compensation is added to the nominal guiding vector field. Particularly, a dynamic scaling mechanism for the wind disturbance compensation is elaborately designed to deal with arbitrarily strong wind conditions. In normal winds, the uniformly ultimately bounded convergence to the desired path can be guaranteed through the stability analysis of the path following error system.

3.1. Wind disturbance estimation

Since the air-flow angles γ_{a} and χ_{a} cannot be directly measured by the onboard sensors, the pitch angle θ and the yaw angle ψ are used to replace γ_{a} and χ_{a}, respectively. Therefore, Eq. (2) is rewritten as

$$\dot{\boldsymbol{P}} = V_{\mathrm{a}}\boldsymbol{v}_1 + \Delta\boldsymbol{f} + \boldsymbol{W} \tag{9}$$

where $\boldsymbol{v}_1 = \mathscr{R}_{\mathrm{b}}^{\mathrm{v}}\boldsymbol{i}$ is treated as the virtual control input for this subsystem, and $\Delta\boldsymbol{f}$ is a modeling error vector introduced by this replacement

$$\begin{aligned} \Delta\boldsymbol{f} &= V_{\mathrm{a}}\left(\mathscr{R}_{\mathrm{a}}^{\mathrm{v}}\boldsymbol{i} - \mathscr{R}_{\mathrm{b}}^{\mathrm{v}}\boldsymbol{i}\right) \\ &= V_{\mathrm{a}}\left(\begin{bmatrix} \cos\gamma_{\mathrm{a}}\cos\chi_{\mathrm{a}} \\ \cos\gamma_{\mathrm{a}}\sin\chi_{\mathrm{a}} \\ -\sin\gamma_{\mathrm{a}} \end{bmatrix} - \begin{bmatrix} \cos\theta\cos\psi \\ \cos\theta\sin\psi \\ -\sin\theta \end{bmatrix}\right) \end{aligned}$$

Although $\Delta\boldsymbol{f}$ is time-varying, its norm is bounded and actually small because the attack and side-slip angles are kept small in the path following flight. We regard the modeling error and the wind as a composite wind disturbance $\boldsymbol{d} = \Delta\boldsymbol{f} + \boldsymbol{W}$. The kinematics in Eq. (2) can be finally rewritten as

$$\dot{\boldsymbol{P}} = V_{\mathrm{a}}\boldsymbol{v}_1 + \boldsymbol{d} \tag{10}$$

The disturbance observer used to estimate the composite wind disturbance $\boldsymbol{d}$ is designed as[25]

$$\begin{cases} \dot{\boldsymbol{z}} = -\boldsymbol{L}\left(V_{\mathrm{a}}\boldsymbol{v}_1 + \hat{\boldsymbol{d}}\right) \\ \hat{\boldsymbol{d}} = \boldsymbol{z} + \boldsymbol{L}\Delta\boldsymbol{P} \end{cases} \tag{11}$$

where $\boldsymbol{z}$ is the internal state of the observer, $\boldsymbol{L} = \mathrm{diag}(l_1,\ l_2,\ l_3) > 0$ is the observer gain matrix and $\Delta\boldsymbol{P}$ denotes the movement from the initial position, i.e., $\Delta\boldsymbol{P} = \boldsymbol{P} - \boldsymbol{P}_0$. $\hat{\boldsymbol{d}}$ is the estimated disturbance vector and the estimation error vector is defined as $\tilde{\boldsymbol{d}} = \boldsymbol{d} - \hat{\boldsymbol{d}}$. Taking the time derivative yields the estimation error dynamics as

$$\dot{\tilde{\boldsymbol{d}}} = -\boldsymbol{L}\tilde{\boldsymbol{d}} + \dot{\boldsymbol{d}} \tag{12}$$

In the conventional DOBC scheme, the estimate is used as a compensation item to reduce the unfavorable influence of disturbance. Intuitively, the straightforward form of desired $\boldsymbol{v}_1$ for Eq. (10) should be

$$\boldsymbol{v}_{1,\,\mathrm{d}} = \frac{1}{V_{\mathrm{a}}}\left(\dot{\boldsymbol{P}}_{\mathrm{d}} - \hat{\boldsymbol{d}}\right) \tag{13}$$

However, we only know the desired direction of $\dot{\boldsymbol{P}}_{\mathrm{d}}$ as given in Eq. (7), but have no specific information about the desired magnitude. Moreover, the practical constraint $\|\ \boldsymbol{v}_1\ \| = \|\ \mathscr{R}_{\mathrm{b}}^{\mathrm{v}}\boldsymbol{i}\ \| = 1$ also requires that the virtual control input satisfies $\|\ \boldsymbol{v}_{1,\,\mathrm{d}}\ \| = 1$. These two problems render it infeasible to apply Eq. (13) directly.

3.2. Wind disturbance compensation under normal winds

Considering that the wind speed is generally in the range of 20%−50% of the airspeed,[6] we make the following assumption at first and call it the normal wind condition.

Assumption 1. The norm of composite wind disturbance $\boldsymbol{d}$ is assumed to be smaller than the airspeed, namely $\| \boldsymbol{d} \| < V_a$.

Remark 2. Since the disturbance observer Eq. (11) is of first-order, which does not exhibit overshoot to a step signal under the zero initial condition, $\| \hat{\boldsymbol{d}} \| <= \| \boldsymbol{d} \|$ is supposed to be valid. Thus, the condition $\| \hat{\boldsymbol{d}} \| < V_a$ can be inferred.

As discussed in Section 3.1, the virtual control input vector $\boldsymbol{v}_1 \in \mathscr{R}^3$ is constrained as $\| \boldsymbol{v}_1 \| = 1$. Given that the path-following control pattern only needs to change the speed direction and has no special requirement for the speed magnitude, to satisfy the constraint, we introduce a scaling factor s to modify the virtual control input Eq. (13) as

$$\boldsymbol{v}_{1,\mathrm{d}} = s\bar{\boldsymbol{P}}_{\mathrm{d}} - \frac{\hat{\boldsymbol{d}}}{V_a} \tag{14}$$

where s adjusts the proportion of $\bar{\boldsymbol{P}}_{\mathrm{d}}$ in the constrained $\boldsymbol{v}_{1,\mathrm{d}}$, and the rest of $\boldsymbol{v}_{1,\mathrm{d}}$ is used to compensate for the composite disturbance. Since $\boldsymbol{v}_{1,\mathrm{d}}$ contains the desired ground speed direction and the wind disturbance compensation, it actually provides a desired airspeed direction command according to the wind triangle.

Substituting Eq. (14) into the magnitude constraint $\| \boldsymbol{v}_{1,\mathrm{d}} \| = 1$ yields

$$\| \bar{\boldsymbol{P}}_{\mathrm{d}}^{\mathrm{v}} \|^2 s^2 - 2\left(\bar{\boldsymbol{P}}_{\mathrm{d}}^{\mathrm{v}}\right)^{\mathrm{T}} \frac{\hat{\boldsymbol{d}}}{V_a} s + \frac{\| \hat{\boldsymbol{d}} \|^2}{V_a^2} - 1 = 0 \tag{15}$$

which is a quadratic equation in terms of the scale factor s. Using $\| \bar{\boldsymbol{P}}_{\mathrm{d}}^{\mathrm{v}} \|^2 = 1$ and the following substitutions

$$b = \frac{\bar{\boldsymbol{P}}_{\mathrm{d}}^{\mathrm{T}} \hat{\boldsymbol{d}}}{V_a},\ c = \frac{\| \hat{\boldsymbol{d}} \|}{V_a}$$

Eq. (15) can be rewritten as

$$s^2 - 2bs + c^2 - 1 = 0 \tag{16}$$

The assumption condition $\| \hat{\boldsymbol{d}} \| < V_a$ is equal to $c^2 - 1 < 0$, which means that this equation must have one positive solution and one negative solution. The positive one is chosen as the scale factor.

$$s^* = c\cos\kappa + \sqrt{1 - c^2 \sin^2\kappa} \tag{17}$$

where $b = c\cos\kappa$ is used and κ is the angle between the two vectors of $\bar{\boldsymbol{P}}_{\mathrm{d}}^{\mathrm{T}}$ and $\hat{\boldsymbol{d}}$, so that actually c and κ are the two independent variables that determine the guidance law Eq. (14).

The convergence to the desired path under the wind disturbance compensated guiding vector field based outer-loop guidance law is concluded in the following theorem.

Theorem 1. Considering the fixed-wing UAV's kinematics Eq. (2), the guiding vector field Eq. (6), the disturbance observer Eq. (11), and the virtual control input Eq. (14) form the outer-loop guidance law. Under Assumption 1, it can be guaranteed that the path following error $\| \boldsymbol{e} \|$ and the disturbance estimation error $\| \tilde{\boldsymbol{d}} \|$ are uniformly ultimately bounded. The errors converge to a residual set that can be made arbitrarily small by adjusting the design parameters.

Proof. First, taking the time derivative of the path following error vector $\boldsymbol{e}(\xi)$ yields

$$\dot{\boldsymbol{e}}(\boldsymbol{\xi}) = \boldsymbol{J}_{\mathrm{e}} \dot{\boldsymbol{\xi}} = \boldsymbol{J}_{\mathrm{e}} \begin{bmatrix} V_a \boldsymbol{v}_1 + \boldsymbol{d} \\ \dot{w} \end{bmatrix} \tag{18}$$

where $\boldsymbol{J}_{\mathrm{e}}$ is the Jacobian matrix of $\boldsymbol{e}(\xi)$ and calculated as

$$\boldsymbol{J}_e = \begin{bmatrix} \nabla^{\mathrm{T}} \varphi_1 \\ \nabla^{\mathrm{T}} \varphi_2 \\ \nabla^{\mathrm{T}} \varphi_3 \end{bmatrix} = \begin{bmatrix} 1 & 0 & 0 & -\tau f_1'(\tau w) \\ 0 & 1 & 0 & -\tau f_2'(\tau w) \\ 0 & 0 & 1 & -\tau f_3'(\tau w) \end{bmatrix}$$

Using the wind disturbance compensated virtual control law Eq. (14) and choosing the dynamics of w as

$$\dot{w} = sV_a \frac{\dot{\boldsymbol{\xi}}_{\mathrm{d}}(4)}{\| \dot{\boldsymbol{\xi}}_{\mathrm{d}}(1:3) \|} \tag{19}$$

the error dynamics of Eq. (18) can be further derived as

$$\begin{aligned} \dot{\boldsymbol{e}}(\boldsymbol{\xi}) &= \boldsymbol{J}_e \begin{bmatrix} V_a \left(s \frac{\dot{\boldsymbol{\xi}}_{\mathrm{d}}(1:3)}{\| \dot{\boldsymbol{\xi}}_{\mathrm{d}}(1:3) \|} - \frac{\dot{\boldsymbol{d}}}{V_a} \right) + \boldsymbol{d} \\ sV_a \frac{\dot{\boldsymbol{\xi}}_{\mathrm{d}}(4)}{\| \dot{\boldsymbol{\xi}}_{\mathrm{d}}(1:3) \|} \end{bmatrix} \\ &= \frac{sV_a}{\| \dot{\boldsymbol{\xi}}_{\mathrm{d}}(1:3) \|} \boldsymbol{J}_e \dot{\boldsymbol{\xi}}_{\mathrm{d}} + \tilde{\boldsymbol{d}} \end{aligned} \tag{20}$$

The definition of the guiding vector field in Eq. (5) can be rewritten in terms of $\boldsymbol{J}_{\mathrm{e}}$ and $\boldsymbol{e}(\xi)$ as

$$\dot{\boldsymbol{\xi}}_{\mathrm{d}} = \times(\rho \nabla \varphi_1,\ \rho \nabla \varphi_2,\ \rho \nabla \varphi_3) - \rho^2 \boldsymbol{J}_e^{\mathrm{T}} \boldsymbol{K} \boldsymbol{e}(\boldsymbol{\xi}) \tag{21}$$

where $\boldsymbol{K} = \mathrm{diag}(k_1,\ k_2,\ k_3)$. By substituting Eq. (21), the dynamics of the path following error $\boldsymbol{e}(\xi)$ can be finally derived as

$$\dot{\boldsymbol{e}}(\boldsymbol{\xi}) = -\frac{sV_a \rho^2}{\| \dot{\boldsymbol{\xi}}_{\mathrm{d}}(1:3) \|} \boldsymbol{J}_e \boldsymbol{J}_e^{\mathrm{T}} \boldsymbol{K} \boldsymbol{e}(\boldsymbol{\xi}) + \tilde{\boldsymbol{d}} \tag{22}$$

The Jacobian matrix $\boldsymbol{J}_{\mathrm{e}} \in \mathscr{R}^{3\times 4}$ has full row rank, so that the matrix $\boldsymbol{J}_e \boldsymbol{J}_e^{\mathrm{T}}$ is positive-definite.

By combining the estimation error dynamics Eq. (12) and the path following error dynamics Eq. (20), the augmented error system is given by

$$\underbrace{\begin{bmatrix} \dot{\boldsymbol{e}} \\ \dot{\tilde{\boldsymbol{d}}} \end{bmatrix}}_{\dot{\boldsymbol{\eta}}} = \underbrace{\begin{bmatrix} -\boldsymbol{\Pi} & \boldsymbol{I} \\ \boldsymbol{0} & -\boldsymbol{L} \end{bmatrix}}_{-\boldsymbol{\Sigma}} \underbrace{\begin{bmatrix} \boldsymbol{e} \\ \tilde{\boldsymbol{d}} \end{bmatrix}}_{\boldsymbol{\eta}} + \begin{bmatrix} \boldsymbol{0} \\ \dot{\boldsymbol{d}} \end{bmatrix} \tag{23}$$

where $\boldsymbol{\Pi} = \frac{sV_a \rho^2}{\| \dot{\boldsymbol{\xi}}_{\mathrm{d}}(1:3) \|} \boldsymbol{J}_e \boldsymbol{J}_e^{\mathrm{T}} \boldsymbol{K}$ is positive-definite and $\boldsymbol{I}$ is a 3×3 unit matrix.

Construct the Lyapunov function as

$$V_1 = \frac{1}{2} \boldsymbol{\eta}^{\mathrm{T}} \boldsymbol{\eta} \tag{24}$$

Taking the time derivative of V_1 yields

$$\begin{aligned}\dot{V}_1 &= -\boldsymbol{\eta}^{\mathrm{T}}\boldsymbol{\Sigma}\boldsymbol{\eta} + \widetilde{\boldsymbol{d}}^{\mathrm{T}}\dot{\boldsymbol{d}} \\ &\leqslant -2\pi_0 V_1 + \widetilde{\boldsymbol{d}}^{\mathrm{T}}\dot{\boldsymbol{d}} \\ &\leqslant -2\pi_0\left(\| \boldsymbol{e} \|^2 + \| \widetilde{\boldsymbol{d}} \|^2\right) + \frac{\beta}{2}\| \widetilde{\boldsymbol{d}} \|^2 + \frac{1}{2\beta}\| \dot{\boldsymbol{d}} \|^2 \\ &\leqslant -\tfrac{1}{2}(4\pi_0 - \beta)V_1 + \tfrac{1}{2\beta}\| \dot{\boldsymbol{d}} \|^2\end{aligned} \tag{25}$$

where $\pi_0 = \lambda_{\min}(\boldsymbol{\Sigma}) > 0$ is the minimum eigenvalue. It can be observed that there must exist a $\beta > 0$ that renders $(4\pi_0 - \beta) > 0$. Consequently, according to Ref. 31, V_1 decreases monotonically until the solution reaches the compact set

$$\Omega_{\mathrm{f}} = \left\{\left(\boldsymbol{e},\ \widetilde{\boldsymbol{d}}\right):\ V_1\left(\boldsymbol{e},\ \widetilde{\boldsymbol{d}}\right) \leqslant V_{\mathrm{f}}\right\}$$

where

$$V_{\mathrm{f}} = \frac{\left\|\dot{\boldsymbol{d}}\right\|^2}{4\pi_0\beta - \beta^2}$$

It can be concluded that the disturbance estimation error $\| \widetilde{\boldsymbol{d}} \|$ and the path following error $\| \boldsymbol{e} \|$ are uniformly ultimately bounded with respect to the bound V_{f}. Note that the maximum value of $4\pi_0\beta - \beta^2$ is $4\pi_0^2$. We can choose relatively larger control gain $\boldsymbol{K}$ and observer gain $\boldsymbol{L}$ to increase π_0. Thus, the errors $\| \widetilde{\boldsymbol{d}} \|$ and $\| \boldsymbol{e} \|$ can converge to an arbitrarily small residual set by increasing π_0. This completes the proof. □

3.3. Wind disturbance compensation expanded to wild winds

In this subsection, we further consider wild wind conditions, for example, wind speed exceeds airspeed, in which the UAV cannot follow the desired path anymore. Assumption 1 is removed and Eq. (14) is extended to cover arbitrarily strong wind fields.

In order to adapt for the wild wind cases, considering the magnitude constraint, another scaling factor r is introduced to reduce the wind disturbance compensation, which gives the modified virtual control input

$$\boldsymbol{v}_{1,\mathrm{d}} = s\dot{\bar{\boldsymbol{P}}}_{\mathrm{d}} - r\frac{\hat{\boldsymbol{d}}}{V_{\mathrm{a}}} \tag{26}$$

Since rejecting the composite wind disturbance is the primary purpose, $r = 1$ is the desired option, which means a full disturbance compensation. The solutions of s and r can be obtained by solving the following constrained optimization problem

$$\mathscr{Q} = \min_{s,\ r}\ (r-1)^2 \tag{27}$$

subject to

$$\begin{cases} \| s\dot{\bar{\boldsymbol{P}}}_{\mathrm{d}} - r\frac{\hat{\boldsymbol{d}}}{V_{\mathrm{a}}} \| = 1 \\ 0 \leqslant r \leqslant 1 \\ 0 \leqslant s \end{cases} \tag{28}$$

where the first equation of Eq. (28) is equal to $s^2 - 2srb + r^2c^2 - 1 = 0$ where b and c have been defined in the last subsection. The second equation of Eq. (28) intends to operate the wind disturbance compensation in a positive range. The third equation of Eq. (28) ensures keeping the direction of the desired ground speed.

Define the Lagrangian function

$$\mathscr{L} = (r-1)^2 + \lambda\left(s^2 - 2srb + r^2c^2 - 1\right) - \mu_1 s - \mu_2 r - \mu_3(1-r) \tag{29}$$

where λ and $\mu_i (i = 1,\ 2,\ 3)$ are the multipliers for Eq. (28). The Karush-Kuhn-Tucker (KKT) conditions are given as[32]

$$\begin{cases} \lambda^*(2s^* - 2br^*) - \mu_1^* = 0 \\ 2(r^* - 1) + \lambda^*(-2bs^* + 2c^2r^*) - \mu_2^* + \mu_3^* = 0 \\ s^{*2} - 2bs^*r^* + c^2r^{*2} - 1 = 0 \\ s^* \geqslant 0,\ r^* \geqslant 0,\ 1 - r^* \geqslant 0 \\ \mu_1^* s^* = 0,\ \mu_2^* r^* = 0,\ \mu_3^*(1 - r^*) = 0 \end{cases} \tag{30}$$

The KKT conditions are always sufficient, so that if s^*, r^*, λ^*, and μ_i^* satisfy the KKT conditions, then s^* and r^* are the optimal solutions for Eqs. (27) and (28). Although generally complicated KKT conditions can only be solved using numerical methods, as to Eq. (30), we can find the analytical solutions via piecewise root-finding.

Case 1. Under the conditions of $0 \leqslant c \leqslant 1,\ \kappa \in [-\pi,\ \pi]$ or $c > 1,\ -\arcsin\frac{1}{c} \leqslant \kappa \leqslant \arcsin\frac{1}{c}$, the optimal solutions can be derived as

$$s^* = c\cos\kappa + \sqrt{1 - c^2\sin^2\kappa},\ r^* = 1,\ \lambda^* = 0,\ \mu_1^* = \mu_2^* = \mu_3^* = 0$$

In this case, $r^* = 1$ makes the full use of the composite wind disturbance estimate $\hat{\boldsymbol{d}}$ and achieves the desired optimal value $\mathscr{Q} = 0$. s^* is the same with Eq. (17). However, compared with the normal wind case discussed in the last subsection, this result extends the assumption $\| \hat{\boldsymbol{d}} \| < V_{\mathrm{a}}$, namely $0 \leqslant c < 1$, to some $c \geqslant 1$ conditions.

Case 2. Under the conditions of $c > 1,\ -\frac{\pi}{2} \leqslant \kappa < -\arcsin\frac{1}{c}$ or $c > 1,\ \arcsin\frac{1}{c} < \kappa \leqslant \frac{\pi}{2}$, the optimal solutions can be derived as

$$s^* = \frac{\cos\kappa}{|\sin\kappa|},\ r^* = \frac{1}{c|\sin\kappa|},\ \lambda^* = \frac{-1 + c|\sin\kappa|}{c^2\sin^2\kappa},\ \mu_1^* = \mu_2^* = \mu_3^* = 0$$

In this case, from $\frac{1}{c} < |\sin\kappa| \leqslant 1$, we have $\frac{1}{c} \leqslant r^* < 1$. Thus, the disturbance estimate $\hat{\boldsymbol{d}}$ can be only partially used to compensate for the excess wind. The optimal value is $\mathscr{Q} = 1 - \frac{1}{c|\sin\kappa|}$, which results in $0 < \mathscr{Q} \leqslant 1 - \frac{1}{c}$.

Case 3. Under the conditions of $c > 1,\ -\pi \leqslant \kappa < -\frac{\pi}{2}$ or $c > 1,\ \frac{\pi}{2} < \kappa \leqslant \pi$, the optimal solutions can be derived as

$$s^* = 0,\ r^* = \frac{1}{c},\ \lambda^* = \frac{1}{c} - \frac{1}{c^2},\ \mu_1^* = -2b\left(\frac{1}{c^2} - \frac{1}{c^3}\right),\ \mu_2^* = \mu_3^* = 0$$

In this case, $s^* = 0$ means the excess wind as well as the large angle κ render that the entire airspeed direction control ability must be used to cope with the wind disturbance. Correspondingly, the optimal value is $\mathscr{Q} = 1 - \frac{1}{c}$.

It is obvious that the optimal value $\mathcal{Q}$ is piecewise continuous. It is assumed that the composite wind disturbance is known. Case 1 is "the normal wind case", where $r^* = 1$ renders that the wind disturbance can be fully compensated. The convergence to the desired path in the normal wind case is proved by Theorem 1. In Case 2 and Case 3, $r^* < 1$ means that the excess wind and the large angle lead to the incomplete compensation for the wind disturbance. We call the two cases "the wild wind cases". Case 2 is a transition state where the UAV cannot keep staying. On the contrary, the persistent excess wind will finally push the UAV into Case 3. Under the conditions of $s = 0$ and $r = \frac{1}{c}$, Eq. (20) becomes $\dot{\boldsymbol{e}}(\xi) = \boldsymbol{d} - r\hat{\boldsymbol{d}} > 0$, which theoretically explains why falling into the wild wind cases implies the divergence of the following error $\| \boldsymbol{e} \|$.

Remark 3. In this work, the proposed wind disturbance compensated guiding vector field can deal with both normal wind cases and wild wind cases in a unified framework, which is why we say that the proposed method is suitable for arbitrarily strong winds. However, given that the fixed-wing UAV needs sufficient forward airspeed to generate lift, there definitely should be limits on the wind. Normally, we can assume that the wind moves mostly in the horizontal plane and the dynamics of the wind is much slower than that of an aircraft. Based on that assumption, the magnitude of the wind can become arbitrarily strong.

4. Inner-loop control design for path following

The wind disturbance compensated guiding vector field, stated in Eq. (26), provides a desired airspeed direction command to the inner-loop. Sequentially, to fulfill the outer-loop guidance command, an inner-loop controller is developed in this section. The backstepping control scheme is employed due to the cascaded dynamics of fixed-wing UAVs.

4.1. Desired attitude angles

The desired airspeed direction guidance signal $\boldsymbol{v}_{1,\mathrm{d}}$ first needs to be transformed to the desired attitude angles. According to $\boldsymbol{v}_1 = \mathscr{R}_{\mathrm{b}}^{\mathrm{v}}\boldsymbol{i}$ in Eq. (9), $\boldsymbol{v}_{1,\mathrm{d}}$ can be regarded as

$$\boldsymbol{v}_{1,\mathrm{d}} = [\cos\theta_{\mathrm{d}}\cos\psi_{\mathrm{d}},\ \cos\theta_{\mathrm{d}}\sin\psi_{\mathrm{d}},\ -\sin\theta_{\mathrm{d}}]^{\mathrm{T}} \tag{31}$$

So that the desired pitch angle can be obtained from the third entry as

$$\theta_{\mathrm{d}} = -\arcsin(\boldsymbol{v}_{1,\mathrm{d}}(3)) \quad \theta_{\mathrm{d}} \in [-0.5\pi,\ 0.5\pi] \tag{32}$$

Define the heading vector in the horizontal plane as $\varepsilon = [\cos\psi,\ \sin\psi]^{\mathrm{T}}$, the desired value of which can also be derived from Eq. (31) as

$$\boldsymbol{\varepsilon}_{\mathrm{d}} = [\cos\psi_{\mathrm{d}},\ \sin\psi_{\mathrm{d}}]^{\mathrm{T}} = \frac{\boldsymbol{v}_{1,\mathrm{d}}(1:2)}{\| \boldsymbol{v}_{1,\mathrm{d}}(1:2) \|} \tag{33}$$

To make the UAV converge to the guiding vector field, consider the following Lyapunov function

$$V_2 = 1 - \varepsilon^{\mathrm{T}}\varepsilon_{\mathrm{d}} \tag{34}$$

Taking the time derivative yields

$$\begin{aligned} \dot{V}_2 &= -\dot{\boldsymbol{\varepsilon}}^{\mathrm{T}}\boldsymbol{\varepsilon}_{\mathrm{d}} - \boldsymbol{\varepsilon}^{\mathrm{T}}\dot{\boldsymbol{\varepsilon}}_{\mathrm{d}} \\ &= -\boldsymbol{\varepsilon}^{\mathrm{T}}\left(\boldsymbol{E}\boldsymbol{\varepsilon}_{\mathrm{d}}\dot{\psi} + \dot{\boldsymbol{\varepsilon}}_{\mathrm{d}}\right) \end{aligned} \tag{35}$$

where $\boldsymbol{E} = \begin{bmatrix} 0 & 1 \\ -1 & 0 \end{bmatrix}$ is a skew-symmetric matrix. By choosing $\boldsymbol{E}\boldsymbol{\varepsilon}_{\mathrm{d}}\dot{\psi} + \dot{\boldsymbol{\varepsilon}}_{\mathrm{d}} = \varepsilon$, $\dot{V}_2 = -\varepsilon^{\mathrm{T}}\varepsilon = -1 < 0$ can be achieved. Therefore, the desired heading rate can be designed as

$$\dot{\psi}_{\mathrm{d}} = \boldsymbol{\varepsilon}_{\mathrm{d}}^{\mathrm{T}}\boldsymbol{E}(-\boldsymbol{\varepsilon} + \dot{\boldsymbol{\varepsilon}}_{\mathrm{d}}) \tag{36}$$

For fixed-wing UAVs, the coordinated turn maneuver is commonly used to change the heading direction. During the coordinated turn, the side-slip angle is kept near zero to eliminate the lateral acceleration and the roll angle ϕ is set so that the horizontal component of the lift force can act as the centripetal force. Therefore, the desired roll angle ϕ_{d} can be approximatively derived as[6]

$$\phi_{\mathrm{d}} = \arctan\frac{V_{\mathrm{a}}\dot{\psi}_{\mathrm{d}}}{g} \quad \phi_{\mathrm{d}} \in (-0.5\pi,\ 0.5\pi) \tag{37}$$

From Eqs. (32), (36), and (37), the desired airspeed direction vector $\boldsymbol{v}_{1,\mathrm{d}}$ has been transformed to the desired pitch angle θ_{d} and roll angle ϕ_{d}.

4.2. Attitude angles and angular rates tracking control

The time derivatives of Euler angles and the rigid-body rotational dynamics are respectively expressed as[6]

$$\underbrace{\begin{bmatrix} \dot{\phi} \\ \dot{\theta} \\ \dot{\psi} \end{bmatrix}}_{\dot{\boldsymbol{x}}_1} = \underbrace{\begin{bmatrix} 1 & \sin\phi\tan\theta & \cos\phi\tan\theta \\ 0 & \cos\phi & -\sin\phi \\ 0 & \sin\phi\sec\theta & \cos\phi\sec\theta \end{bmatrix}}_{\boldsymbol{G}(\boldsymbol{x}_1)} \underbrace{\begin{bmatrix} p \\ q \\ r \end{bmatrix}}_{\boldsymbol{x}_2} \tag{38}$$

$$\boldsymbol{J}\dot{\boldsymbol{x}}_2 = -\boldsymbol{x}_2 \times \boldsymbol{J}\boldsymbol{x}_2 + \boldsymbol{M} \tag{39}$$

where $\boldsymbol{x}_1 = [\phi,\ \theta,\ \psi]^{\mathrm{T}}$ is the Euler angle vector, $\boldsymbol{x}_2 = [p,\ q,\ r]^{\mathrm{T}}$ is the body frame angular rate vector, $\boldsymbol{J}$ is the inertial matrix, and $\boldsymbol{M} \in \mathbb{R}^3$ is the external moment vector.

Given that the roll and pitch angles are independently controlled in the coordinated turn flight, the attitude angle tracking error vector is defined as

$$\boldsymbol{\delta}_1 = \boldsymbol{z}_1 - \boldsymbol{z}_{1,\mathrm{d}}, \boldsymbol{z}_1 = [\phi,\ \theta]^{\mathrm{T}}, \boldsymbol{z}_{1,d} = [\phi_{\mathrm{d}},\ \theta_{\mathrm{d}}]^{\mathrm{T}} \tag{40}$$

where

$$\boldsymbol{z}_1 = \begin{bmatrix} 1 & 0 & 0 \\ 0 & 1 & 0 \end{bmatrix}\boldsymbol{x}_1 = \boldsymbol{H}\boldsymbol{x}_1 \tag{41}$$

The angular rate tracking error vector is defined as

$$\boldsymbol{\delta}_2 = \boldsymbol{x}_2 - \boldsymbol{x}_{2,\mathrm{d}} \tag{42}$$

where $\boldsymbol{x}_{2,\mathrm{d}}$ denotes the desired angular rate, which is the virtual control input for the attitude angle tracking.

Applying the backstepping design procedure, the first-step Lyapunov function is defined as[33]

$$V_3 = \frac{1}{2}\boldsymbol{\delta}_1^{\mathrm{T}}\boldsymbol{\delta}_1 \tag{43}$$

Taking the time derivative yields

$$\begin{aligned} \dot{V}_3 &= \boldsymbol{\delta}_1^{\mathrm{T}}(\dot{\boldsymbol{z}}_1 - \dot{\boldsymbol{z}}_{1,\mathrm{d}}) \\ &= \boldsymbol{\delta}_1^{\mathrm{T}}[\boldsymbol{H}\boldsymbol{G}(\boldsymbol{\delta}_2 + \boldsymbol{x}_{2,\mathrm{d}}) - \boldsymbol{H}\dot{\boldsymbol{x}}_{1,\mathrm{d}}] \end{aligned} \tag{44}$$

The desired angular rate can be designed as

$$\boldsymbol{x}_{2,\mathrm{d}} = \boldsymbol{G}^{-1}\left(\begin{bmatrix} -c_1\boldsymbol{\delta}_1 \\ 0 \end{bmatrix} + \begin{bmatrix} \dot{\boldsymbol{z}}_{1,\mathrm{d}} \\ \dot{\psi}_{\mathrm{d}} \end{bmatrix}\right) \quad c_1 > 0 \tag{45}$$

where the desired heading rate $\dot{\psi}_{\mathrm{d}}$ is specially designed to achieve the coordinated turn as

$$\dot{\psi}_{\mathrm{d}} = \frac{g}{V_{\mathrm{a}}}\tan\phi_{\mathrm{d}} + k_y A_y \tag{46}$$

where A_y is the lateral acceleration in the body frame, and the item $k_y A_y$ is used to damp the side-slip angle to zero. By substituting Eq. (45), $\dot{V}_3$ in Eq. (44) can be further derived as

$$\dot{V}_3 = \boldsymbol{\delta}_1^{\mathrm{T}}\boldsymbol{H}\boldsymbol{G}\boldsymbol{\delta}_2 - c_1\boldsymbol{\delta}_1^{\mathrm{T}}\boldsymbol{\delta}_1 \tag{47}$$

In the second-step, the Lyapunov function is sequentially chosen as

$$V_4 = V_3 + \frac{1}{2}\boldsymbol{\delta}_2^{\mathrm{T}}\boldsymbol{\delta}_2 \tag{48}$$

Taking the time derivative yields

$$\begin{aligned}\dot{V}_4 &= \dot{V}_3 + \boldsymbol{\delta}_2^{\mathrm{T}}\dot{\boldsymbol{\delta}}_2 \\ &= \dot{V}_3 + \boldsymbol{\delta}_2^{\mathrm{T}}\left[\boldsymbol{J}^{-1}(-\boldsymbol{x}_2\times\boldsymbol{J}\boldsymbol{x}_2 + \boldsymbol{M}) - \dot{\boldsymbol{x}}_{2,\mathrm{d}}\right]\end{aligned} \tag{49}$$

To stabilize the error dynamics, the actual control input is designed as

$$\boldsymbol{M} = \boldsymbol{J}\left(-c_2\boldsymbol{\delta}_2 + \dot{\boldsymbol{x}}_{2,\mathrm{d}} - \boldsymbol{G}^{\mathrm{T}}\boldsymbol{H}^{\mathrm{T}}\boldsymbol{\delta}_1\right) + \boldsymbol{x}_2\times\boldsymbol{J}\boldsymbol{x}_2 \quad c_2 > 0 \tag{50}$$

By substituting Eq. (50) into Eq. (49), $\dot{V}_3$ can be derived as

$$\dot{V}_4 = -c_1\boldsymbol{\delta}_1^{\mathrm{T}}\boldsymbol{\delta}_1 - c_2\boldsymbol{\delta}_2^{\mathrm{T}}\boldsymbol{\delta}_2 \leqslant 0 \tag{51}$$

Since the two-step backstepping control law in Eqs. (45) and (50) is constructed along with the control Lyapunov functions, the inner-loop closed-loop system is globally asymptotically stable and the global convergence to the desired roll angle ϕ_{d} and pitch angle θ_{d} is achieved.

Remark 4. The time derivative values $\dot{\varepsilon}_{\mathrm{d}}$, $\dot{\boldsymbol{z}}_{1,\mathrm{d}}$, and $\dot{\boldsymbol{x}}_{2,\mathrm{d}}$ can be calculated using the filtering methods such as the dynamic surface,[34] the command filter,[20] or the differentiator.[35]

The overall structure of the proposed path following control strategy combining the outer-loop and the inner-loop can be summarized in the block diagram shown in Fig. 2.

Remark 5. The overall system is not in the form of a chain of integrators due to the transformation from $\boldsymbol{v}_{1,\mathrm{d}}$ to ϕ_{d} and θ_{d}. Therefore, the cascaded controllers Eqs. (26), (45), and (50) are constructed partially following the standard backstepping technique. Although it is not a straightforward task to establish the stability of the overall system by using a single Lyapunov function, we can still guarantee the stability by exploiting the natural time-scale separation property between the system dynamics.

5. Simulation studies

To evaluate the performance of the proposed wind disturbance compensated guiding vector field, numerical simulations of normal and wild wind conditions are carried out based on the full 6-DOF model of Aerosonde UAV described in Ref. 6.

The wind disturbance $\boldsymbol{W}$ in Eq. (2) is modeled as a steady wind $\boldsymbol{W}_{\mathrm{s}} \in \mathscr{R}^3$ with the added random turbulence $\boldsymbol{W}_{\mathrm{r}} \in \mathscr{R}^3$. The mathematical expressions for $\boldsymbol{W}_{\mathrm{r}}$ are given by the Dryden transfer functions as[6]

$$\begin{cases} H_u(s) = \sigma_u\sqrt{\frac{2V_{\mathrm{a}}}{L_u}}\cdot\frac{1}{s+\frac{V_{\mathrm{a}}}{L_u}} \\ H_v(s) = \sigma_v\sqrt{\frac{3V_{\mathrm{a}}}{L_v}}\cdot\frac{s+\frac{V_{\mathrm{a}}}{\sqrt{3}L_v}}{\left(s+\frac{V_{\mathrm{a}}}{L_v}\right)^2} \\ H_w(s) = \sigma_w\sqrt{\frac{3V_{\mathrm{a}}}{L_w}}\cdot\frac{s+\frac{V_{\mathrm{a}}}{\sqrt{3}L_w}}{\left(s+\frac{V_{\mathrm{a}}}{L_w}\right)^2} \end{cases}$$

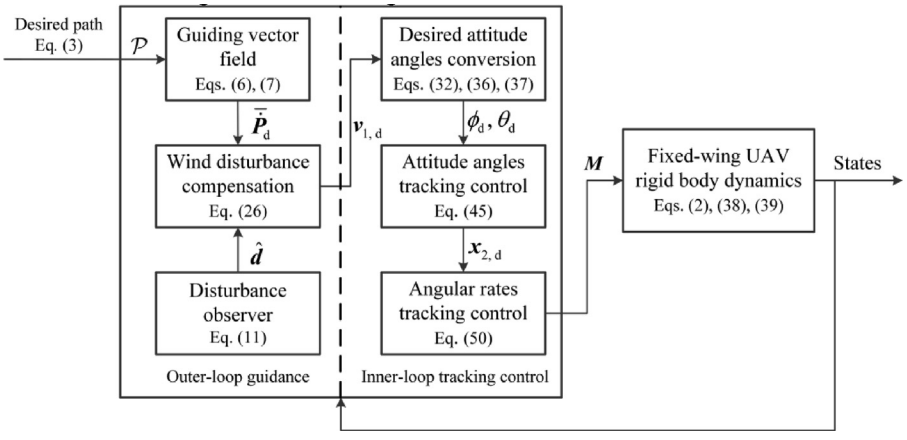

Fig. 2 Structure of path following control strategy.

where σ_u, σ_v, σ_w and L_u, L_v, L_w are the intensities and spatial wavelengths of the turbulence along the body frame axes, respectively.

To further illustrate the robustness of the proposed method and make the simulation results more credible, sensor noises are also present. By applying the error-state Kalman filter introduced in Ref. 36, the vehicle states can be estimated from the measurements of accelerometer, rate gyro, pitot-static probe, and GNSS. The GNSS data are updated at 1 Hz. The measurement errors are assumed to be Gaussian random noises and the corresponding standard deviations are listed in Table 1.

Table 2 lists the conditions and parameters used in simulations.

5.1. Normal wind case for helical path

In the first scenario of normal wind, a w-parameterized 3D helical path, according to Eq. (3), is used as the reference path

$$\mathscr{P}_1 = \{x = 150\cos(-0.1w),\ y = -150\sin(-0.1w),\ z = -20w\}$$

where the radius and the slope of this helix are 150 m and 4/3, respectively.

The whole simulation time is set to 120 s. The steady wind is first imposed as $\boldsymbol{W}_s = [10,\ 10,\ 5]^T$ m/s at 20 s, and then changed to the opposite direction. Considering that the airspeed is independently kept at $V_a = 30$ m/s, the steady wind magnitude $\| \boldsymbol{W}_s \| = 15$ m/s counts for 50% of the airspeed, which is quite severe in a normal flight. Initially, the UAV is located on the path to eliminate the initial path following error, for we simply want to evaluate the robustness of the proposed wind disturbance compensated guiding vector field.

The original ground speed based guiding vector field proposed by Ref. 9 is applied as a comparison. The inner-loop structure of the original guiding vector field based path following control algorithm is the same with the proposed one, except that γ takes the place of θ in $\boldsymbol{z}_1$ defined in Eq. (40) and V_a is substituted by V_g in Eq. (46).

At first, an overall glance at the 3D flight paths in Fig. 3 reveals that the path following control algorithm using the proposed wind disturbance compensated Guiding Vector Field (GVF) achieves better following accuracy than the one using the original GVF. To be specific, the time histories of the path following error components, represented by functions $\varphi_i (i = 1,\ 2,\ 3)$, are shown in Fig. 4. During the wind period, from 20 s to 100 s, it can be observed that the curves representing the proposed GVF algorithm show smaller offset errors in all three components. The performance indexes of the Euclidean norm of the error vector $\boldsymbol{e} = [\varphi_1,\ \varphi_2,\ \varphi_3]^T$ are summarized in Table 3. According to the statistics, the proposed path following algorithm using the wind disturbance compensated guiding vector field improves the mean error and the standard deviation of the path offset by 47% and 53% compared with the original guiding vector field based algorithm, which indicates that the proposed wind disturbance compensated guiding vector field achieves better robustness in the normal wind condition.

Table 1 Gaussian random noise parameters.

Sensor	Standard deviation of random noise
Accelerometer (m/s^2)	0.025
Rate gyro (°/s)	0.13
Pressure sensors (Pa)	Absolute pressure: 10 Differential pressure: 2
GNSS (m)	Horizontal position: 2.5 Altitude: 5

Table 2 Simulation settings.

Sensor	Parameter	Value
Flight conditions	Airspeed (m/s)	30
	Constraints for θ_d (°)	±60
	Constraints for ϕ_d (°)	±60
Controller parameters	k_1, k_2, k_3	0.005
	ρ	0.1
	$\boldsymbol{L}$	diag (1, 1, 3)
	c_1, c_2	3, 6
GNSS	σ_u, σ_v, σ_w (m/s)	1.06, 1.06, 0.7
	L_u, L_v, L_w (m)	200, 200, 50

Particularly, to further analyze the differences, we perform the simulation that measurement noises are not included. That is to say, all the true values of the states are used. The time history results are shown in Fig. 5 and the performance indexes from 20 s to 100 s are summarized in Table 4. Although the proposed GVF algorithm achieves slightly better performance in the horizontal plane, the original GVF algorithm clearly overtakes the advantage in the vertical direction. This is because the original GVF algorithm uses the true value of γ in the inner-loop vertical control. In contrast, as stated in Eq. (9), θ is used instead of γ to represent the virtual control input in the proposed GVF algorithm, so that the modeling error leads to the accuracy loss in the vertical direction. As a result, the mean errors of the two algorithms are 2.94 m versus 2.70 m. Considering that the path radius is 150 m, this difference is too small to distinguish. Thus, we can say that theoretically, by using the true state values, these two path following algorithms can achieve the same level of accuracy in normal wind conditions. However, the flight-path angle γ is determined via GNSS data and actually not available on most low-cost autopilots due to its low quality. Compare with the results in Fig. 4 and Table 3, which are obtained with sensor noises. The mean error of the proposed GVF algorithm increases from 2.94 m to 9.07 m, whereas that of the original GVF algorithm surges to 17.16 m from 2.70 m. It can be inferred that although sensor noises amplify the path following errors of both algorithms, the proposed wind disturbance compensated guiding vector field has better noise tolerance and achieves smaller following error, which makes it more suitable for small-scale low-cost fixed-wing UAVs.

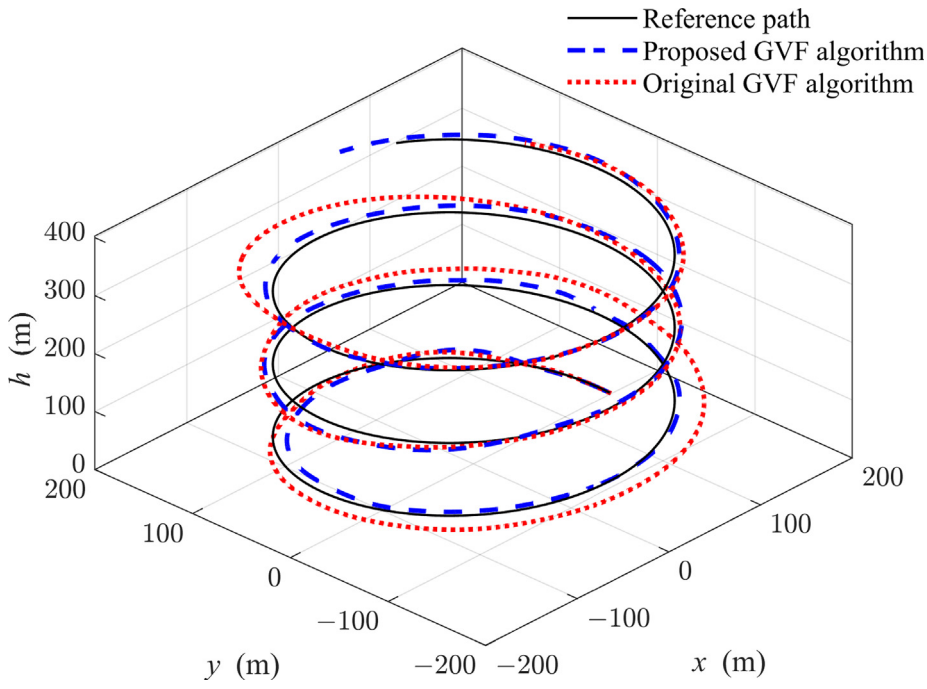

Fig. 3 3D helical ascending path following.

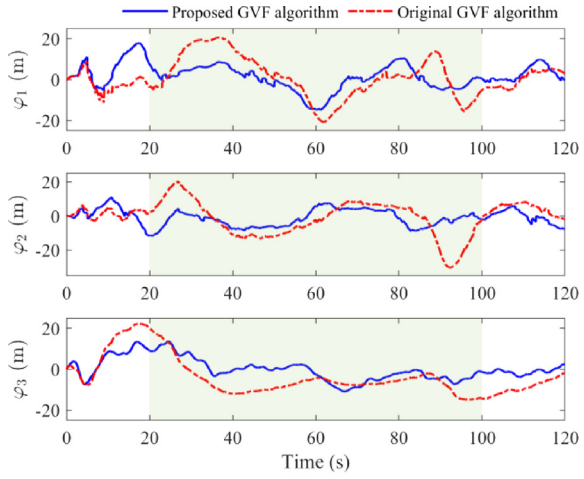

Fig. 4 Following error components for helical path.

The composite wind disturbance estimation is shown in Fig. 6. It can be observed that when there are no measurement noises, an accurate and rapid estimation can be obtained for the composite wind disturbance. Obviously, measurement noises degrade the estimation performance, especially in the beginning before the Kalman filter has converged.

The time histories of the scaling factors s and r (with measurement noises) are depicted in Fig. 7. As analyzed in Section 3.3, for normal wind cases, the full compensation for the wind disturbance can be achieved, so that the scaling factor r is 1 all the time. As expected, the scaling factor s works properly to enlarge or reduce the normalized desired ground speed vector.

Table 3 Following accuracy indexes for helical path.

Algorithm	Maximum (m)	Mean (m)	Standard deviation (m)
Proposed GVF algorithm	16.52	9.07	2.99
Original GVF algorithm	32.26	17.16	6.47

5.2. Normal wind case for Lissajous path

The proposed algorithm is also tested on another w-parameterized 3D Lissajous path

$$\mathscr{P}_2 = \{x = 320\cos(-0.1w),\ y = 280\sin(-0.2w),\ z = -50\cos(-0.2w)\}$$

This path, which is also used in Ref. 9, is eight-shaped in the horizontal plane and bent along the vertical axis.

To avoid repetitive descriptions, the simulation conditions of time, wind disturbance, and measurement noises are set as the same with those in the last scenario. The results of 3D flight paths, time histories of the following error components, and following accuracy indexes from 20 s to 100 s are demonstrated in Fig. 8, Fig. 9, and Table 5, respectively. It can be observed that the proposed GVF algorithm can also achieve good following accuracy for the following accuracy indexes do not differ significantly compared with those of the helix scenario. In contrast, the original GVF algorithm performs much worse for the mean error increases by about 79% from 17.16 m to 30.68 m. Especially, as shown in Fig. 9, the large error can be seen in the vertical direction, which implies that the perfor-

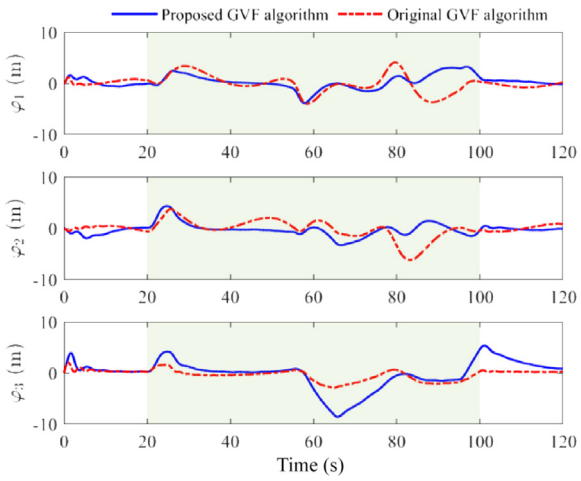

Fig. 5 Following error components for helical path using true state values.

Table 4 Following accuracy indexes for helical path using true state values.

Algorithm	Maximum (m)	Mean (m)	Standard deviation (m)
Proposed GVF algorithm	9.15	2.94	2.36
Original GVF algorithm	6.23	2.70	1.59

mance of the original GVF algorithm is critically dependent on the data quality of the flight-path angle.

5.3. Wild wind case

In the third scenario, the steady wind soars to $\| \boldsymbol{W}_s \| = 34$ m/s, i.e., $\| \boldsymbol{W}_s \| > V_a$, which means that the wild wind case defined in Section 3.3 may be activated. We verify the effectiveness of the proposed wind disturbance compensated guiding vector field in preventing run-away from the desired path. Likewise, the geometric guidance law for wild wind conditions proposed by Ref. 26 is employed as a comparison, which is designed as

$$\boldsymbol{v}_{1,\mathrm{d}} = \frac{\sqrt{\| \hat{\boldsymbol{d}} \|^2 - V_a^2} \bar{\boldsymbol{P}}_{\mathrm{d}} - \hat{\boldsymbol{d}}}{\| \sqrt{\| \hat{\boldsymbol{d}} \|^2 - V_a^2} \bar{\boldsymbol{P}}_{\mathrm{d}} - \hat{\boldsymbol{d}} \|} \tag{52}$$

Usually, the wild wind does not last long so that the UAV is expected to stay stable during the excess wind and quickly recover from drifting after that. In order to stimulate the wild wind conditions $c > 1$ and $|\kappa| > \arcsin\frac{1}{c}$, we assume that the horizontal steady wind with the speed of 34 m/s comes from four different directions. The measurement noises are also included.

The original guiding vector field based path following algorithm used in the previous simulation cannot maintain a stable flight in the wild winds because insisting on tracking the desired ground speed direction will persistently give large attitude commands that cause the inner-loop to lose stability. Thus, only the results under the proposed GVF algorithm and the geometric algorithm based on Eq. (52) are shown in Fig. 10. It can be seen that in each condition the UAV is pushed away from the desired path by the wild wind. Comparing the time histories of the horizontal deviations from the desired circle path given in Fig. 11, the proposed GVF algorithm clearly outperforms the geometric algorithm and demonstrates much smaller deviations in the last three wind conditions. For the first wind condition of $\boldsymbol{W}_s = [24,\ 24,\ 0]^{\mathrm{T}}$ m/s, the proposed GVF algorithm shows larger deviation at first, but its deviation rate is smaller than that of the geometric algorithm so that an overturn can be seen at about 50 s. Fig. 12 shows the time histories of the scaling factors under four conditions, respectively. The scaling factor r is always below 1 in all four conditions, which explains that the wind disturbance estimate is scaled down to satisfy the magnitude constraint and the partial wind compensation causes the UAV to deviate from the desired path. Meanwhile, the scaling factor s falls to 0

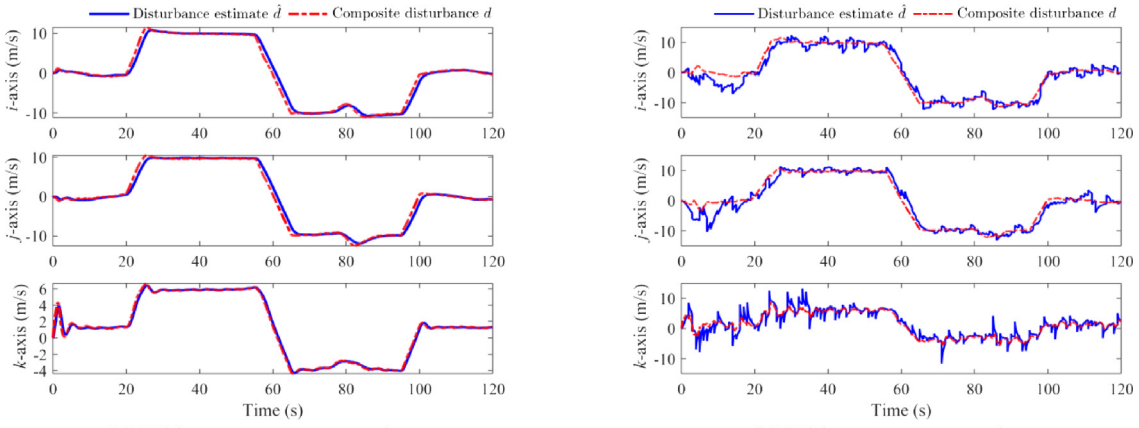

(a) Without measurement noises (b) With measurement noises

Fig. 6 Composite wind disturbance estimation.

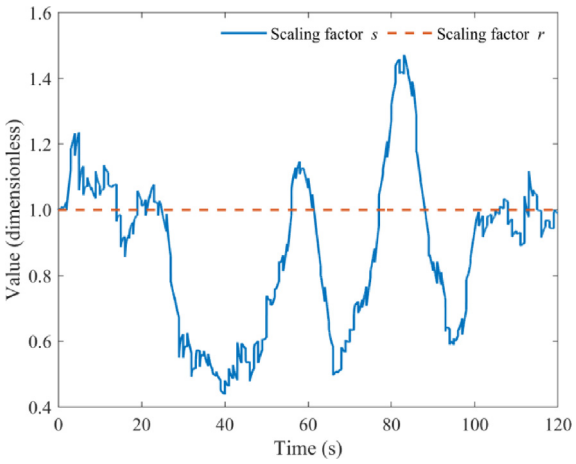

Fig. 7 Scaling factors in normal wind case.

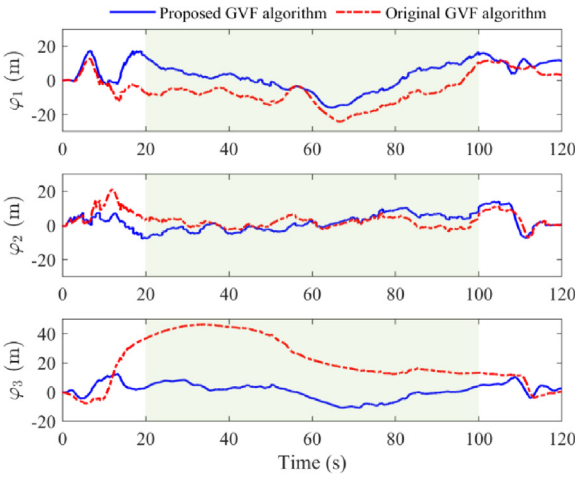

Fig. 9 Following error components for Lissajous path.

in all four conditions, which verifies that the wild wind Case 2 cannot hold as discussed in Section 3.3. $s = 0$ means that the proposed GVF algorithm cannot spare any control effort to track the desired ground speed direction and heading against the wind direction is the optimal action to minimize the deviation.

6. Conclusions

This paper proposes a novel path following control strategy based on the wind disturbance compensated guiding vector field to improve the performance of low-speed fixed-wing UAVs in various wind conditions. This approach can not only achieve better sensor noise tolerance and following accuracy in normal winds, but also maintain a smaller deviation from the desired path in wild winds. The reason behind the advantages lies in that the two scaling factors are introduced to dynamically enlarge or reduce the nominal guiding vector field and the feed-forward wind disturbance compensation in the DOBC scheme for the first time. Moreover, an optimal problem is

Table 5 Following accuracy indexes for Lissajous path.

Algorithm	Maximum (m)	Mean (m)	Standard deviation (m)
Proposed GVF algorithm	18.87	9.74	4.35
Original GVF algorithm	46.91	30.68	11.83

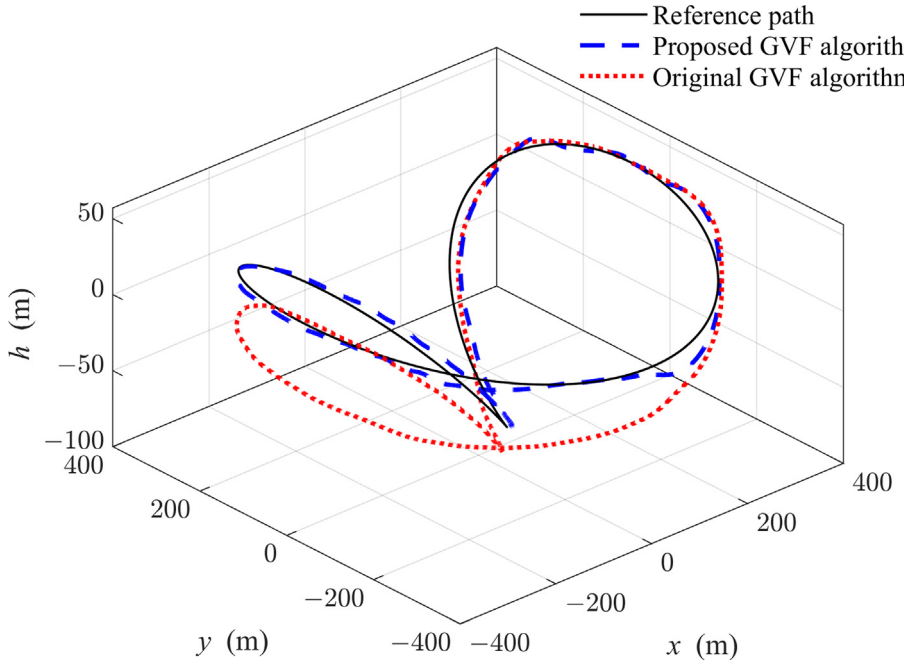

Fig. 8 3D Lissajous path following.

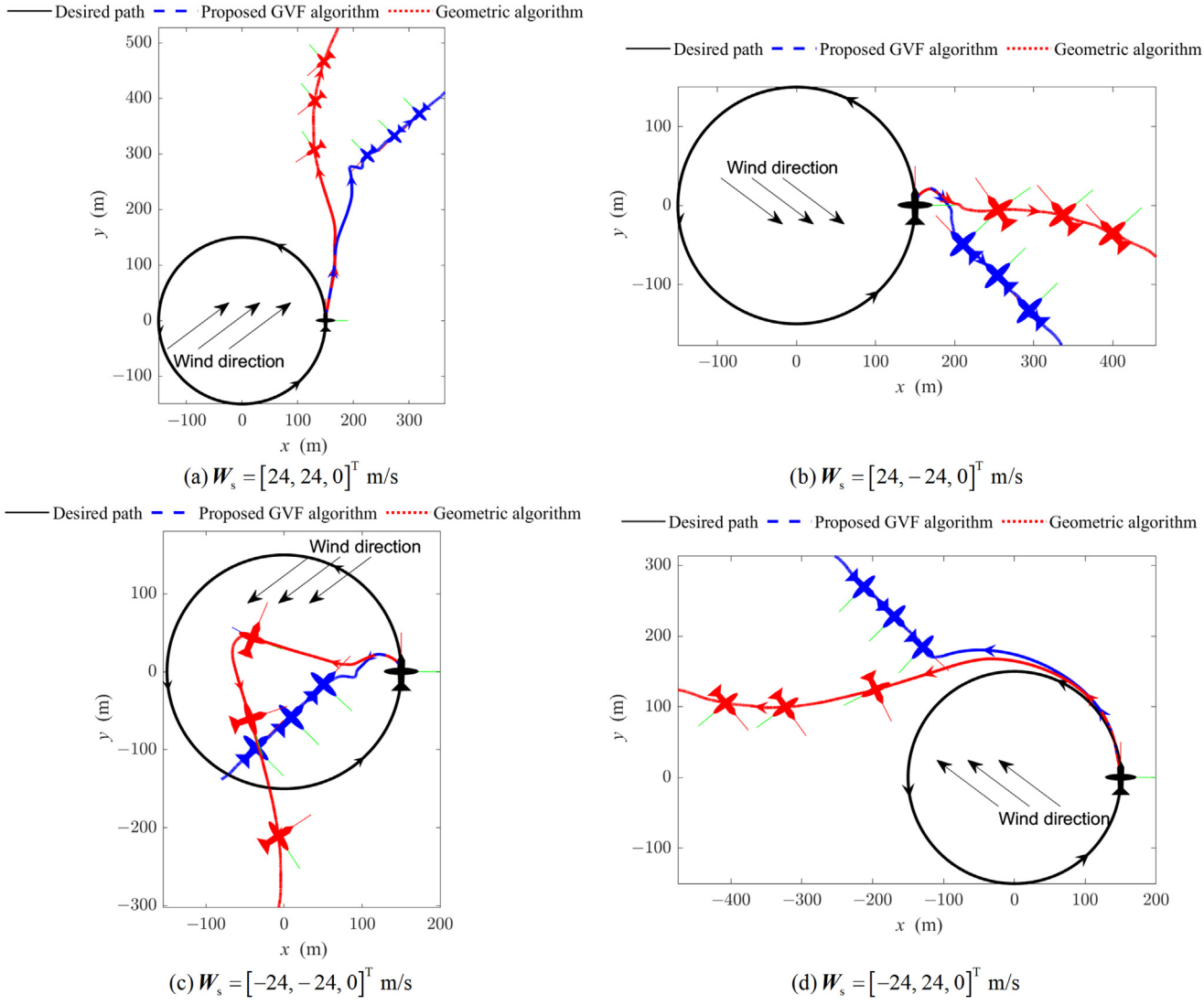

Fig. 10 Flight paths under four wild wind conditions.

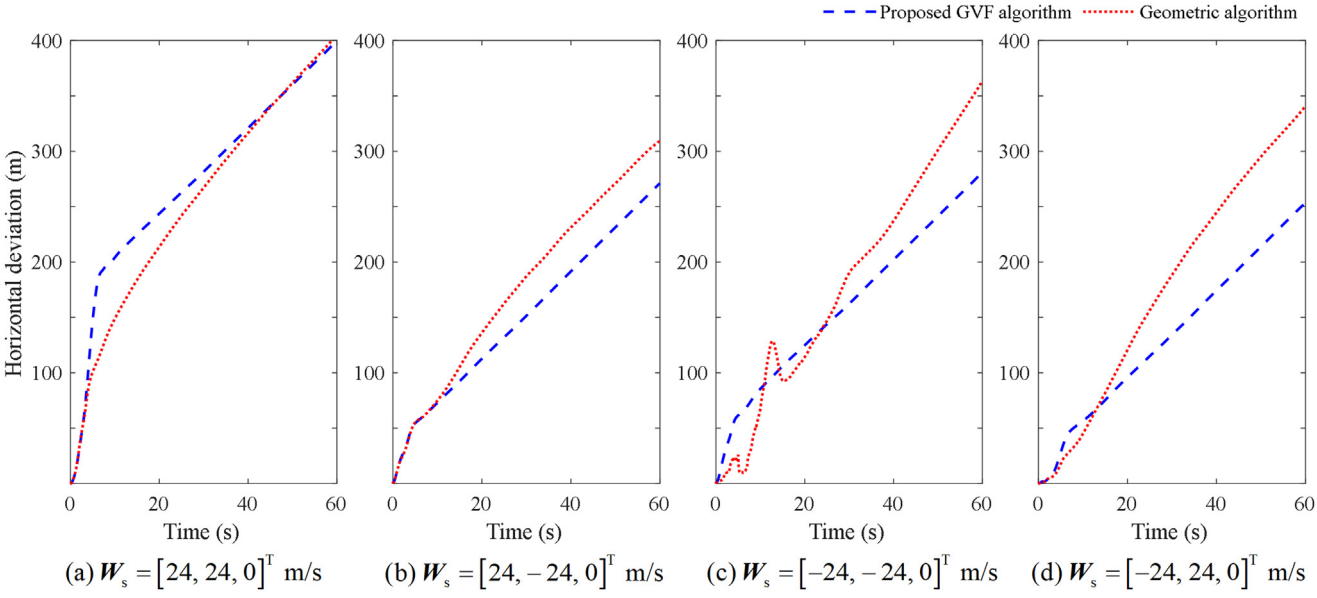

Fig. 11 Horizontal deviations under four wild wind conditions.

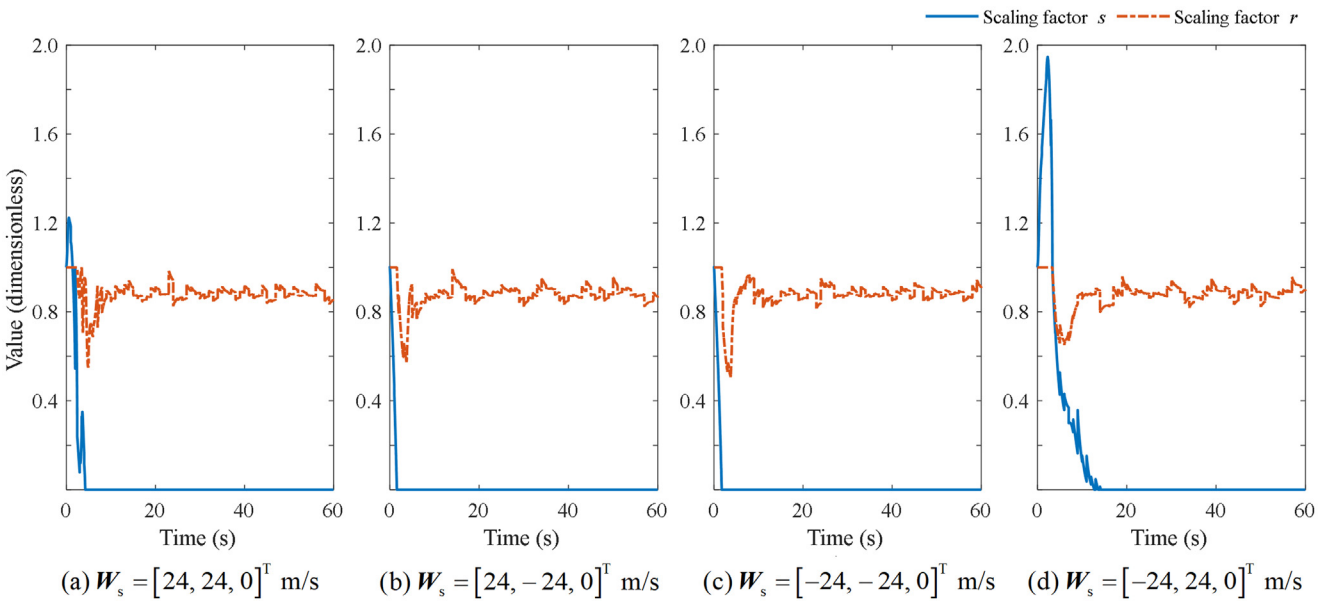

Fig. 12 Scaling factors under four wild wind conditions.

constructed to guarantee that the limited control effort is used in preference for wind disturbance compensation, from which the scaling factors can be explicitly calculated based on the KKT conditions. Numerical simulations with various performance comparisons are carried out to validate the effectiveness of the proposed algorithm. This method may be of particular interest in the flight control application for low-speed, low-cost fixed-wing UAVs.

Declaration of competing interest

The authors declare that they have no known competing financial interests or personal relationships that could have appeared to influence the work reported in this paper.

Acknowledgements

This study was co-supported by the National Natural Science Foundation of China (Nos. 62273024, 62203034, 62073096, and 62073016), the Zhejiang Provincial Natural Science Foundation of China (No. LZ22F030012), and The Heilongjiang Touyan Team Program, China.

References

1. Aguiar AP, Hespanha JP, Kokotović PV. Performance limitations in reference tracking and path following for nonlinear systems. *Automatica* 2008;**44**(3):598–610.
2. Matschek J, Bäthge T, Faulwasser T, et al. Nonlinear predictive control for trajectory tracking and path following: An introduction and perspective. *Handbook of Model Predictive Control*. Cham: Birkhäuser; 2019. p. 169–98.
3. Sujit PB, Saripalli S, Sousa JB. Unmanned aerial vehicle path following: A survey and analysis of algorithms for fixed-wing unmanned aerial vehicles. *IEEE Contr Syst Mag* 2014;**34**(1):42–59.
4. Xavier DM, Silva NBF, Branco KRLJC. Path-following algorithms comparison using software-in-the-loop simulations for UAVs. *J Intell Rob Syst* 2022;**106**(3):63.
5. Hung N, Rego F, Quintas J, et al. A review of path following control strategies for autonomous robotic vehicles: Theory, simulations, and experiments. *J Field Robot* 2023;**40**(3):747–79.
6. Beard RW, McLain TW. Small unmanned aircraft. Princeton: Princeton University Press; 2012.
7. Wang YJ, Wang XK, Zhao SL, et al. Vector field based sliding mode control of curved path following for miniature unmanned aerial vehicles in winds. *J Syst Sci Complex* 2018;**31**(1):302–24.
8. Yao WJ, Cao M. Path following control in 3D using a vector field. *Automatica* 2020;**117**:108957.
9. Yao WJ, de Marina HG, Lin BH, et al. Singularity-free guiding vector field for robot navigation. *IEEE Trans Rob* 2021;**37**(4):1206–21.
10. Yao WJ, Lin BH, Anderson BDO, et al. The domain of attraction of the desired path in vector-field guided path following. *IEEE Trans Autom Contr* 2023;**99**:1–8.
11. Gao ZX, Fu J. Robust LPV modeling and control of aircraft flying through wind disturbance. *Chin J Aeronaut* 2019;**32**(7):1588–602.
12. de Marina HG, Kapitanyuk YA, Bronz M, et al. Guidance algorithm for smooth trajectory tracking of a fixed wing UAV flying in wind flows. *2017 IEEE international conference on robotics and automation (ICRA)*. Piscataway: IEEE Press; 2017. p. 5740–5.
13. Wu WN, Wang Y, Gong CL, et al. Path following control for miniature fixed-wing unmanned aerial vehicles under uncertainties and disturbances: A two-layered framework. *Nonlinear Dyn* 2022;**108**(4):3761–81.
14. Souanef T. L_1 adaptive path-following of small fixed-wing unmanned aerial vehicles in wind. *IEEE Trans Aerosp Electron Syst* 2022;**58**(4):3708–16.
15. Hamada Y, Tsukamoto T, Ishimoto S. Receding horizon guidance of a small unmanned aerial vehicle for planar reference path following. *Aerosp Sci Technol* 2018;**77**:129–37.
16. Borup KT, Fossen TI, Johansen TA. A nonlinear model-based wind velocity observer for unmanned aerial vehicles. *IFAC-PapersOnLine* 2016;**49**(18):276–83.

17. Liu CJ, McAree O, Chen WH. Path-following control for small fixed-wing unmanned aerial vehicles under wind disturbances. *Int J Robust Nonlinear Control* 2013;**23**(15):1682–98.
18. Yang J, Liu CJ, Coombes M, et al. Optimal path following for small fixed-wing UAVs under wind disturbances. *IEEE Trans Contr Syst Technol* 2020;**29**(3):996–1008.
19. Song YP, Yong KN, Wang XL. Disturbance interval observer-based robust constrained control for unmanned aerial vehicle path following. *Drones* 2023;**7**(2):90.
20. Lu H, Liu CJ, Guo L, et al. Flight control design for small-scale helicopter using disturbance-observer-based backstepping. *J Guid Contr Dyn* 2015;**38**(11):2235–40.
21. Guo KX, Jia JD, Yu X, et al. Multiple observers based anti-disturbance control for a quadrotor UAV against payload and wind disturbances. *Contr Eng Pract* 2020;**102**:104560.
22. Yan YD, Liu CJ, Oh H, et al. Dual-layer optimization-based control allocation for a fixed-wing UAV. *Aerosp Sc Technol* 2021;**119**:107184.
23. Cui YY, Qiao JZ, Zhu YK, et al. Velocity-tracking control based on refined disturbance observer for gimbal servo system with multiple disturbances. *IEEE Trans Ind Electron* 2022;**69**(10):10311–21.
24. Liu ZB, Zhu YK, Qiao JZ. Composite anti-disturbance position and attitude control for spacecrafts with parametric uncertainty and flexible vibration. *Chin J Aeronaut* 2022;**35**(12):242–52.
25. Chen WH, Yang J, Guo L, et al. Disturbance-observer-based control and related methods—An overview. *IEEE Trans Ind Electron* 2015;**63**(2):1083–95.
26. Furieri L, Stastny T, Marconi L, et al. Gone with the wind: Nonlinear guidance for small fixed-wing aircraft in arbitrarily strong windfields. *2017 American control conference (ACC)*. Piscataway: IEEE Press; 2017. p. 4254–61.
27. Stastny T, Siegwart R. On flying backwards: Preventing run-away of small, low-speed, fixed-wing UAVs in strong winds. *2019 IEEE/RSJ international conference on intelligent robots and systems (IROS)*. Piscataway: IEEE Press; 2020. p. 5198–205.
28. Galffy A, Böck M, Kugi A. Nonlinear 3D path following control of a fixed-wing aircraft based on acceleration control. *Contr Eng Pract* 2019;**86**:56–69.
29. Kai JM, Hamel T, Samson C. A unified approach to fixed-wing aircraft path following guidance and control. *Automatica* 2019;**108**:108491.
30. Seo Y, Kim Y. Flight dynamics of aerial vehicle considering time-varying ambient wind. *Aerosp Sci Technol* 2022;**126**:107601.
31. Wang CL, Wen CY, Guo L. Decentralized output-feedback adaptive control for a class of interconnected nonlinear systems with unknown actuator failures. *Automatica* 2016;**71**:187–96.
32. Boyd S, Vandenberghe L. *Convex optimization*. Cambridge: Cambridge University Press; 2004.
33. Van Ekeren W, Looye G, Kuchar R, et al. Design, implementation and flight-test of incremental backstepping flight control laws. Reston: AIAA; 2018. Report No.: AIAA-2018-0384.
34. Hou MZ, Liang XL, Duan GR. Adaptive block dynamic surface control for integrated missile guidance and autopilot. *Chin J Aeronaut* 2013;**26**(3):741–50.
35. Lu Y. Disturbance observer-based backstepping control for hypersonic flight vehicles without use of measured flight path angle. *Chin J Aeronaut* 2021;**34**(2):396–406.
36. Solà J. Quaternion kinematics for the error-state Kalman filter. arXiv preprint: 1711.02508; 2017.